The TRIple-frequency and Polarimetric radar Experiment for improving process observation of winter precipitation

José Dias Neto[1], Stefan Kneifel[1], Davide Ori[1], Silke Trömel[2], Jan Handwerker[3], Birger Bohn[4],
Normen Hermes[5], Kai Mühlbauer[2], Martin Lenefer[2], and Clemens Simmer[2]

[1]Institute for Geophysics and Meteorology, University of Cologne, Cologne, Germany
[2]Meteorological Institute, University of Bonn, Bonn, Germany.
[3]Institute of Meteorology and Climate Research (IMK), Karlsruhe Institute of Technology (KIT), Karlsruhe, Germany
[4]Institute of Energy and Climate Research (IEK-8), Research Centre Jülich, Jülich, Germany
[5]Institute of Bio- and Geosciences Agrosphere (IBG-3), Research Centre Jülich, Jülich, Germany

Correspondence: José Dias (jdiasnet@uni-koeln.de)

Abstract. This study describes a two-months dataset of ground-based triple-frequency (X, Ka, and W-Band) Doppler cloud radar observations during the winter season obtained at the Jülich ObservatorY for Cloud Evolution core facility (JOYCE-CF), Germany. All relevant post-processing steps, such as re-gridding, offset and attenuation correction as well as quality flagging are described. The dataset contains all information needed to recover data at intermediate processing steps for user-specific applications and corrections (DOI: 10.5281/zenodo.1405539). The rather long time duration of the dataset allowed for a statistical analysis, which we focused on the ice and snow part of the cloud. The reflectivity differences quantified by dual-wavelength ratios revealed temperature regimes, where aggregation seems to be triggered. Overall, the aggregation signatures found in the triple-frequency space agree with and corroborate conclusions from previous studies. Combining the information from reflectivity information with mean Doppler velocity and linear depolarization ratio, enables us to distinguish signatures of rimed particles and melting snowflakes; while the riming signatures agree well with results from previous studies, we find very strong aggregation signatures close to the melting layer, which have not been reported before. Mean Doppler velocity and the linear depolarization ratio have been used to separate the extreme aggregation signature from the triple-frequency characteristics of melting particles.

Copyright statement. TEXT

1 Introduction

The combined observation of clouds and precipitation at different radar frequencies potentially improves the particle type and quantity retrieval accuracy because their scattering and absorption properties depend on the particle microphysical characteristics and electromagnetic frequency. One example is the retrieval of vertical profiles of cloud liquid water content from the differential radar attenuation at 35 and 94 GHz (e.g. Hogan et al. (2005)) and the retrieval of precipitation rates from the

Ku-Ka-Band dual-frequency radar on the core satellite of the Global Precipitation Mission (GPM, Hou et al. (2014)). For frequencies below ≈10 GHz, attenuation effects are very small (except for heavy rainfall or hail) but the sensitivity to non-precipitating particles is weak. Therefore, the majority of multi-frequency applications for cold clouds focus on cloud radar systems operating usually at 35 GHz or 94 GHz which provide enhanced sensitivity even to sub-millimeter ice particles and

5 cloud droplets. The microwave scattering properties of frozen hydrometeors such as snowflakes, graupel, and hail lie in this frequency range within the transition zone between Rayleigh and Mie scattering regimes. Thus, this size-dependent scattering effect can be used to improve the estimates of ice water content and characteristic particle size distribution (PSD) (Matrosov, 1998; Hogan et al., 2000).

Recent modeling studies (Kneifel et al., 2011b; Tyynelä and Chandrasekar, 2014; Leinonen and Moisseev, 2015; Leinonen

10 and Szyrmer, 2015) revealed that different ice particle classes like graupel, single crystals, or aggregates, can be distinguished using a combination of three radar frequencies (13, 35 and 94 GHz). Early triple-frequency radar datasets from airborne campaigns (Leinonen et al., 2012; Kulie et al., 2014) confirmed distinct signatures of the various ice hydrometeor classes in the triple frequency space. Ground-based triple-frequency radar measurements in combination with in-situ observations (Kneifel et al., 2015) provided the experimental evidence for a close relation between triple-frequency signatures and the characteristic

15 particle size as well as the bulk density of snowfall. Methods which utilize the information content of the triple-frequency Doppler spectrum are still under development but first analyses show already their potential e.g. to constrain snow particle scattering models (Kneifel et al., 2016).

In this article, we present a first analysis of two months winter triple-frequency (X, Ka, W-Band) radar observations collected at the Jülich observatory for cloud evolution core facility, Germany (Löhnert et al., 2015). Particular effort has been taken to

20 correct the data for known offsets and attenuation as well as to re-grid the dataset to allow its convenient use for multi-frequency analyses. Section 2 describes the experimental campaign and the characteristics of the X, Ka and W band radars used during the experiment. Section 3 gives a detailed description of the data processing, corrections applied and remaining limitations of the data. Section 4 presents a statistical analysis of the data where a temperature dependency of the triple-frequency signatures is identified. In addition, signatures of riming and melting snow particles are presented.

25 2   Measurement Site and Instruments

The "TRIple-frequency and Polarimetric radar Experiment for improving process observation of winter precipitation" (TRIPEx) was a joint field experiment of the University of Cologne, the University of Bonn, the Karlsruhe Institute of Technology (KIT), and the Jülich Research Centre (FZJ). TRIPEx took place at the Jülich Observatory for Cloud Evolution Core Facility (JOYCE-CF, $50°54'31''N, 6°24'49''E$, 111 m above mean sea level; Löhnert et al. (2015)) from 11 November 2015 until 04 January

30 2016. The core instruments deployed during TRIPEx were three vertically pointing radars providing a triple-frequency (X-Band, Ka-Band, and W-Band) column view of the hydrometeors aloft. Figure 1 shows a simplified diagram of the instruments relative deployment positions. In addition to the three radars, a large number of permanently installed remote sensing and in-situ observing instruments are available at the JOYCE-CF site (see Löhnert et al. (2015) for a detailed overview).
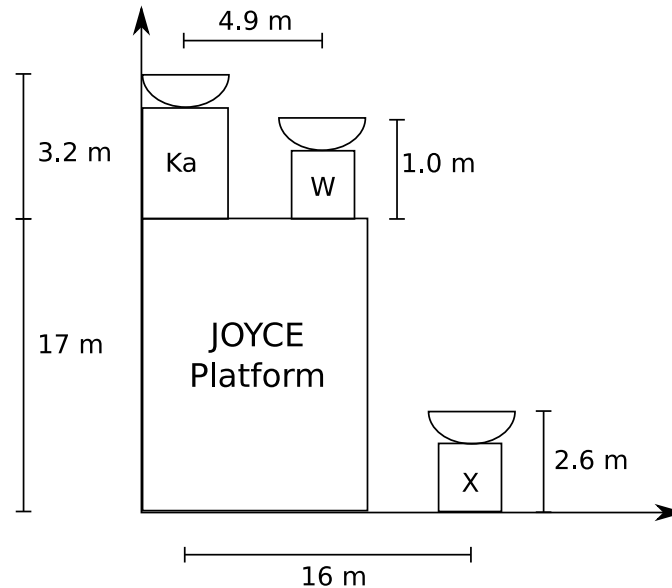
Figure 1. Sketch (not to scale) of the horizontal and vertical distances of the three zenith-pointing radars operated during TRIPEx. The JOYCE-CF platform with all auxiliary instruments is located on the roof of a 17 m tall building. The mobile X-Band radar was placed on the ground as close as possible to the other two radars.

2.1 Precipitation Radar KiXPol (X-Band)

KiXPol is a pulsed X-band Doppler precipitation radar, normally integrated into the KITcube platform (Kalthoff et al., 2013). The mobile Meteor 50DX radar, manufactured by Selex ES (Gematronik), is mounted on a trailer and placed next to the JOYCE-CF building in order to position it as close as possible to the other two radars which were installed on the JOYCE-CF

5   roof-platform (see Figure 1). KiXPol operates at 9.4 GHz in a simultaneous transmit and receive (STAR) mode and is thus capable to measure standard polarimetric variables like differential reflectivity Z_{dr} and differential phase shift Φ_{dp}, but not the linear depolarization ratio LDR which requires the emission of single-polarization pulses in order to allow for independent measurements of the cross-polarized component of the returning signal. Due to the zenith only operation during the campaign, the KiXPol polarimetric variables available from its STAR-mode operation do not contain relevant information about the

10   hydrometeors and are thus not included in the dataset. Using a pulse duration of 0.3 µs, we set the radial resolution down to 30 m which is close to the resolution of the other radars (see Table 1). Since KiXPol is designed for operational observations of precipitation via volume scans (series of azimuth scans at several fixed elevation angles) the standard software requires to rotate the antenna in azimuth in order to record data. Hence, we constantly rotated the antenna at zenith elevation with a slow rotation speed ($2°\text{s}^{-1}$) in order to enhance the sensitivity due to longer time averaging. After each complete rotation, a gap of

15   a few seconds interrupts the measurement before the next scan was started. Further technical specifications about the KiXPol can be found in Table 1.

2.2 Cloud Radar JOYRAD-35 (Ka-Band)

JOYRAD-35 is a scanning Ka-Band Doppler cloud radar of the type MIRA-35 (Görsdorf et al., 2015) manufactured by METEK Meteorologische Messtechnik GmbH, Germany. An overview of its main technical characteristics and settings used during TRIPEx is provided in Table 1. JOYRAD-35 transmits linearly polarized pulses at 35.5 GHz and receives simultaneously the co- and cross-polarized returns; thus the linear depolarization ratio LDR can be derived, which is used e.g. to filter out signals from insects and to detect the melting layer by the Metek processing software. From the measured Doppler spectra, standard radar moments such as effective reflectivity factor Ze, mean Doppler velocity MDV and Doppler spectral width SW are computed. Since March 2012, JOYRAD-35 is a permanent component of the JOYCE-CF site (Löhnert et al., 2015) and its zenith observations are used as input for generating CloudNet products (Illingworth et al., 2007). As the main scientific focus during TRIPEx was to collect combined triple-frequency observations, JOYRAD-35 was vertically pointing most of the time. Every 30 minutes it performed a sequence of Range Height Display (RHI) scans at different azimuth directions (duration $\approx$ 4 minutes) in order to capture a snapshot of the spatial cloud field and also to derive horizontal wind inside the cloud. As the scanning data has not been processed yet, the current dataset only includes the zenith observations and the RHI scans will be included in a future release. JOYRAD-35 was almost continuously operating during the TRIPEx campaign, except a gap from 25th of November to 2[sd] of December 2015 that was related to a hard disk failure.

2.3 Cloud Radar JOYRAD-94 (W-Band)

JOYRAD-94 is a 94 GHz frequency modulated continuous wave (FMCW) radar combined with a radiometric channel at 89 GHz manufactured by Radiometer Physics GmbH (RPG), Germany. Unlike the previously introduced two radars, JOYRAD-94 is a non-polarimetric, non-scanning and non-pulsed radar system. JOYRAD-94 is continuously operating at JOYCE-CF since October 2015; a detailed description of the radar performance, hardware, signal processing, and calibration can be found in Küchler et al. (2017). As summarized in Table 1, JOYRAD-94 has a similar beam-width as well as range and temporal resolution as JOYRAD-35. Unlike for the pulsed radars, the JOYRAD-94 range resolution is not fixed, but depends on the gate distance as a consequence of the use of different FMCW chirp settings for different heights. We used the standard chirp table (Table 2) as described in Küchler et al. (2017) which has different range resolutions, Nyquist velocities, and sensitivities for the different height ranges. The measured Doppler spectra are first corrected for aliasing (Küchler et al., 2017), and standard radar moments such as equivalent Ze, MDV and SW are derived from them.

3 Data processing

The TRIPEx dataset is stored in three different levels of processing. Level 0 contains the original data from JOYRAD-35, JOYRAD-94 and KixPol. For Level 1 the measurements were corrected for known instrument problems and were formatted into a common time-height grid. At this stage, the data can be still considered raw; further processing steps that are either dependent on electromagnetic frequency or atmospheric conditions are applied to the Level 2 dataset. These processing

Table 1. Technical specifications and settings of the three vertically pointing radars operated during TRIPEx at JOYCE-CF.

Specifications	KiXPol	JOYRAD-35	JOYRAD-94
Frequency [GHz]	9.4	35.5	94.0
3dB Beam Width [°]	1.3	0.6	0.5
Sensitivity at 5km [dBZ][a]	-14	-42	-39
Nyquist Velocity [$\pm$ms^{-1}]	9	10	4.2 - 9.7[b]
Range Resolution [m]	30.0	28.8	16 - 34.1[b]
Temporal Sampling [s]	1	2	3
Lowest clutter-free range [m]	700	400	370
Radome	Yes	No	Yes

[a] Minimum sensitivities have been derived from the reflectivity histograms shown in Fig. 6.

[b] Nyquist velocity and range resolution depend on the chirp definition; those values are indicated in Table 2.

Table 2. Main settings of the chirp table used during TRIPEx for the JOYRAD-94. (see Küchler et al. (2017) for a detailed description of the JOYRAD-94 chirp table)

Attributes	Chirp sequence			
	1	2	3	4
Integration Time [s]	0.338	0.402	0.530	1.769
Range Interval [m]	100 - 400	400 - 1200	1200 - 3000	3000 - 12000
Range Resolution [m]	16.0	21.3	26.9	34.1
Nyquist Velocity [$\pm$ms^{-1}]	9.7	8.1	6.2	4.2
Doppler FFT	512	512	512	512

steps include the exclusion of measurements affected by ground clutter, the relative calibration of the radars with independent sources, the compensation for estimated differential attenuation due to atmospheric gases, the cross-calibration among the three radars and the addition of data quality flags. These processing steps are meant to remove spurious multi-frequency signals that are not connected with cloud microphysical processes. The processing is performed to the best of our knowledge, however, the intermediate transformations are kept within the database, allowing us to recover the data at any stage and possibly apply different processing techniques. Figure 2 illustrates the work-chain from Level 0 to Level 2. A detailed description of each step is provided in the following sections.

3.1 Spatio-temporal re-gridding and offset correction

As shown in Table 1, the range and temporal resolution of the three radars are slightly different. The data are re-gridded on a common time and space domain in order to derive e.g. dual wavelength ratios DWRs which is defined for two wavelengths $\lambda 1$,
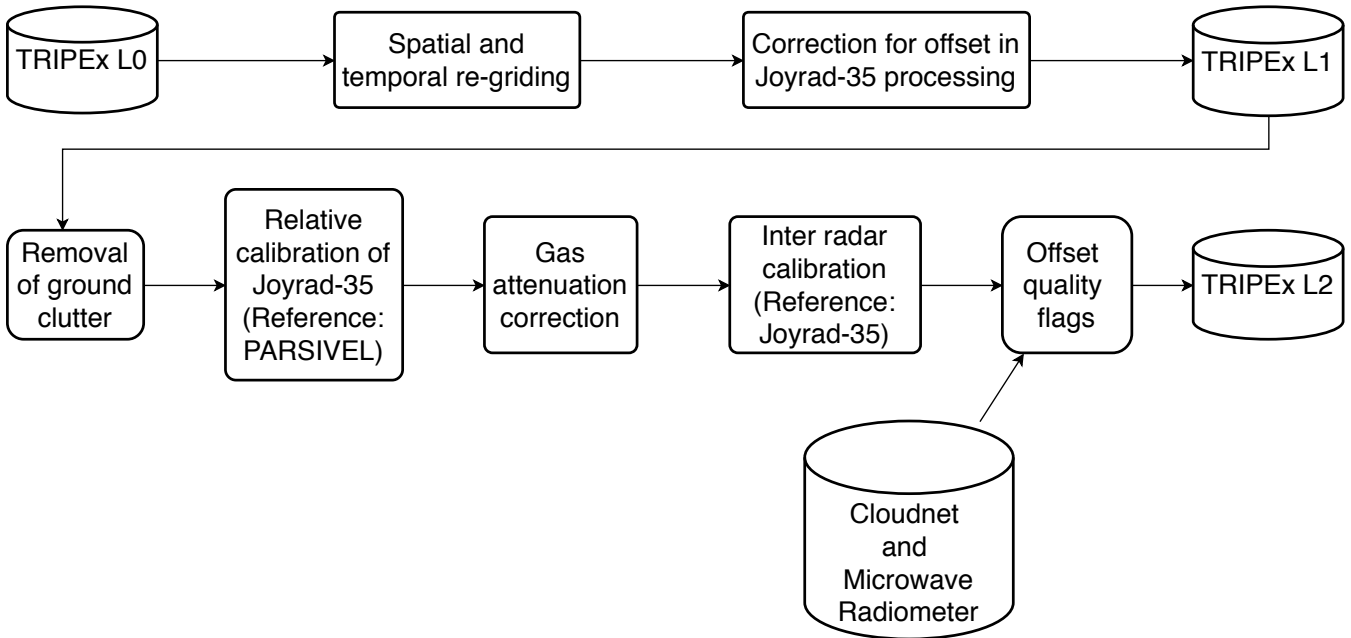
Figure 2. Flowchart of the TRIPEx data processing. The upper part describes the steps applied for the data Level 1 and the bottom part describes the steps applied for the data Level 2 product which is the product used in this study.

$\lambda 2$ as

$$\mathrm{DWR} = \mathrm{Ze}_{\lambda 1} - \mathrm{Ze}_{\lambda 2} \tag{1}$$

where Ze_{λ} is in dBZ. To this goal, we first defined a reference grid with a base temporal resolution of 4 s and a vertical resolution of 30 m which is close to the original data resolution; the reference of the new height grid is the altitude of the W-
Band radar. The data values are interpolated using a *nearest neighbour* approach and the maximum data displacement is limited to ± 17 m in range and ± 2 s in time. Using the nearest-neighbour method ensures to conserve the high resolution information of the original radar observations. The reason for limiting the interpolation displacement is to avoid spurious multi-frequency features, that may result from non-matching radar volumes. Effects of the residual volume mismatch occur at cloud boundaries where cloud heterogeneity is most prominent. For JOYRAD-35 we also applied two corrections to the original radar moments as suggested by the manufacturer (Matthias Bauer-Pfundstein, Metek GmbH, personal communication): in order to account for power loss due to the finite receiver bandwidth, an offset of 2 dB has been added. In addition, in order to correct for an issue in the Digital Signal Processor used in older MIRA systems another 3 dB offset to the JOYRAD-35 reflectivity factors has been added. We apply these corrections to Ze for processing of the Level 1 data.

3.2 Evaluation of the JOYRAD-35 calibration with PARSIVEL disdrometer measurements

For the Level 1 processing we accounted for known radar offsets and re-gridded the data onto a common time-height grid. In the following steps, we calibrate the three radars relatively to each other and estimate the quality based on the applied corrections. Our relative calibration approach follows the previous triple-frequency study by Kneifel et al. (2015)). First, radar gates affected by ground clutter are detected and removed from the database according to the height thresholds listed in Table 1. For the relative calibration we take JOYRAD-35 as reference, because of its better sensitivity level compared to KiXPol up to high elevations and its lower signal attenuation compared to W-Band. Moreover, JOYRAD-35 is the only system not equipped with a radome which might collect raindrops on its surface and cause additional attenuation. We also expect that signal attenuation due to antenna wetness on JOYRAD-35 to be lower because of the periodic antenna tilts during RHI scans.

In order to evaluate the quality of the JOYRAD-35 calibration, we compared the reflectivities measured at 500 - 600 m with those derived from drop size distributions (DSD) observed by a co-located Parsivel optical disdrometer (Löffler-Mang and Joss (2000)) during three light rainfall events. The scattering properties of raindrops have been computed using the T-matrix approach (Leinonen, 2014) assuming a drop shape model that follows Thurai et al. (2007) and a Gaussian distribution of canting angles with zero mean and $7°$ standard deviation (Huang et al., 2008). The Parsivel was unfortunately not functioning during the TRIPEx campaign itself, hence we did the comparison for two cases before and one case after the campaign. These precipitation events lasted for several hours and provided thus meaningful statistics. The frequency distributions of the reflectivities measured by JOYRAD-35 and calculated using T-matrix are shown in Figure 3. While the overall shapes of the two histograms are very similar, the mean values from JOYRAD-35 are in every case approximately 4 dB lower than the those derived from the T-matrix model. This persistency suggests a bias due to radar miscalibration, which we corrected accordingly in the JOYRAD-35 dataset being aware of the caveats of radar-disdrometer comparisons.

3.3 Correction for atmospheric gas attenuation

Hydrometeors and atmospheric gases cause considerable attenuation at cloud radar frequencies. We correct for estimated attenuation due to atmospheric gases (Fig. 2) by means of the Passive and Active Microwave TRAnsfer model (PAMTRA) (Maahn et al., 2015). PAMTRA calculates specific attenuation due to molecular nitrogen, oxygen and water vapour based on the gas absorption model from Rosenkranz (1998). Input parameters are the vertical profiles of atmospheric temperature, pressure and humidity provided by the CloudNet product (Illingworth et al., 2007), which is generated operationally at the JOYCE-CF site. The two-way path integrated attenuation (PIA) at the radar range gates is derived from the specific attenuation integrated along the vertical. Table 3 lists the minimum and maximum two way attenuation values at ≈ 12 km (height of the maximum range gate in Level 2 data) for the three radars during the entire campaign. The highest attenuation of ≈ 2.6 dB - mainly caused by water vapor - occurs at 94 GHz. The lowest maximum attenuation of ≈ 0.1 dB is found for 9.4 GHz, which is mainly produced by oxygen continuum absorption. At 35.5 GHz, where attenuation is governed by both oxygen and water vapour, the maximum attenation is ≈ 0.7 dB and thus between those found at 9.4 GHz and 94 GHz.
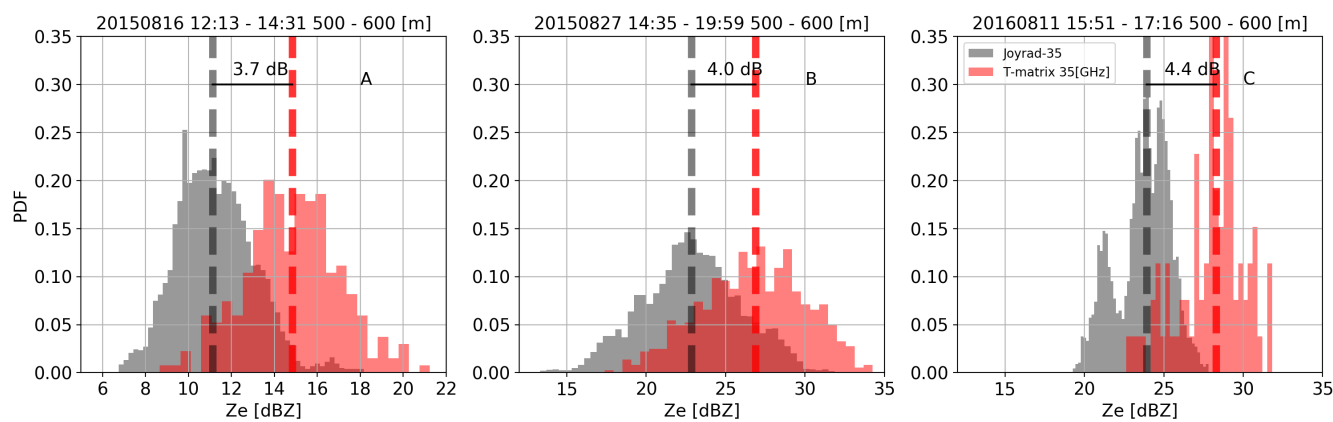
Figure 3. Histograms of radar reflectivities from JOYRAD-35 (gray) and T-matrix calculation with the rain drop size distribution provided by Parsivel (red) for three long-lasting stratiform rain cases before and after the TRIPEx campaign (16 August 2015 (A), 27 August 2015 (B), 11 August 2016 (C)). JOYRAD-35 reflectivities are taken from the lowest clutter-free range gates between 500 and 600 m. The vertical dashed line indicates the median of the distribution; the offset is calculated as the difference between JOYRAD-35 and T-matrix results.

Table 3. Calculated minimum and maximum two-way path integrated attenuation (PIA) at a height of ≈ 12 km for X-, Ka-, and W-Band during TRIPEx.

Frequency [GHz]	Minimum Attenuation [dB]	Maximum Attenuation [dB]
9.4	0.077	0.104
35.5	0.365	0.728
94	0.650	2.675

3.4 Inter radar calibration and generation of quality flags

Spurious non-physical multi-frequency signals can arise from attenuation effects due to particulate atmospheric components (e.g., liquid water, melting layer, snow), but also from instrument specific effects such as wet radome, snow on the antenna, and remaining relative offsets due to radar mis-calibration. The last step in the Level 2 processing is an estimate of the relative

5 offset among the three radars. The processing is complemented by a series of quality flags categorized as errors and warnings. Error flags mark data affected by a poor quality of the applied correction procedure, and the warnings indicate the detection of potential sources of inter-radar offsets that are not accounted for in the procedures described below. An additional error flag is raised if spurious multi-frequency signals due to radar volume mismatch are suspected.

Following the methodologies applied by Kneifel et al. (2015) and Hogan et al. (2000), we assume that small ice particles

10 in the upper parts of the cloud are mostly Rayleigh scatterers; thus their reflectivities should not be frequency dependent (Matrosov, 1993). We estimate the reflectivity range, for which we can make this assumption, by investigating the behaviour of the respective DWRs as function of Ze_{Ka}. The uncorrected DWRs are expected to remain constant within the Rayleigh

regime and start to deviate from that value when particles in the resepective radar volumes enter the Mie regime first for the higher-frequency radar. Separate reflectivity thresholds are needed for X and W-Band since the transition into Mie scattering is expected to happen at larger Ze for X-Band than for W-Band. In addition, the sensitivity of the X-Band is much lower and thus we need to accept a larger reflectivity threshold for the offset estimate between X and Ka-Band. For the relative offset

5   estimate of the W-band radar, we found an optimal range of $-30 < Ze_{Ka} < -10$ dBZ, while for the X-band radar the range of $-20 < Ze_{Ka} < -5$ dBZ was used. In order to safely exclude partially melted particles, we only use reflectivities from at least 1 km above the 0 °C isotherm.

The relative offset correction is estimated for each time instant based on the data of a moving time window of 15 minutes centered over that time instant and restricted to reflectivity pairs, which obey the previously stated conditions. The mean value

10   of the DWR computed for these reflectivity pairs constitutes the relative inter radar offset. The quality of the relative offset correction strongly depends on the quality and quantity of the reflectivity data included in the moving time window. A large number of data points spanning through many reflectivity values within the Rayleigh regime is required in order to reliably estimate the relative offset between the radars. Estimates from less than 300 valid reflectivity pairs might contain large sampling errors. Moreover, in regions close to cloud edges or for Ze close to the sensitivity limits of the radars, the statistical correlation

15   of the two reflectivities strongly deteriorate. Thus, we flag time periods characterized by reflectivity correlations below 0.7 or number of valid reflectivity pairs below 300 as unreliable. The two criteria for the offset quality are stored separately as error quality flags (see Table 4).

Table 4. Quality flags included in the data Level 2 product (bit-coded in a 16-bit integer value). The flags indicate the reliability of the data and in particular the applicability of the relative offset estimate for X-Ka and W-Ka band reflectivities. Note that offsets are not calculated, when the number of reflectivity pairs is below 300.

	Bits	Criteria
Warning	0-5	Reserved for future warning flags
	6	LWP >200 gm^{-2}
	7	Rain detected by CloudNet
Errors	8-12	Reserved for future error flags
	13	Variance in time of DWR >2 dB^2
	14	Correlation of data points is poor (<0.7)
	15	Number of valid measurements <300

The described correction technique accounts for all processes, which affect relative offsets of the radars in the upper, frozen part including possible frequency-dependent attenuation effects occurring at lower levels besides radar miscalibration and

20   radome/antenna attenuation. Since the estimated correction is, however, applied to the entire profile inevitably an overcompensation will occur in the lower rainy part. Thus, the data should only be used for the ice part of the cloud, for which microwave attenuation can be considered negligible, and which was the main focus of the campaign. Differential attenuation in the ice part of the cloud can, however, be generated by super-cooled liquid drops; thus the subsequent analysis of the DWR signal in that

part of the cloud might be affected by this error. Especially for rain and melting layer studies or when information about amount and position of super-cooled liquid water is available, e.g. form lidar or radar Doppler spectra, a refined correction can and should be applied. Additional warning flags indicate periods with larger liquid water path derived from the nearby microwave radiometer or the occurrence of rainfall and/or a melting layer from the CloudNet classification and the precipitation gauge,

5   and are summarized in Table 4.

Despite the technically optimal match of the different frequency radar volumes, mismatches are unavoidable due to the horizontal distances between the radars (Figure 1), the different radar range resolutions and beam widths (Table 1). At cloud edges and close to the melting layer, where the largest spatial cloud inhomogeneities can be expected, the impact of the remaining radar volume mismatch on the DWRs will be maximum. We used the temporal variability of the DWRs estimated

10 from 2-minutes moving windows as an indicator for potential volume mismatch. Cloud regions with variances above 2 dB^2 are flagged. Filtering of these data reduces the scatter of data in the triple-frequency space, but also might remove interesting data from regions with strong signal gradients.

3.4.1   Example of data filtering based on quality flags

The effect of the different quality flag and additional filtering approaches on DWR_{XKa} and DWR_{KaW} is demonstrated for the

15 clouds observed on 20.11.2015 in Figure 4 and 5. For a better visualization the filtering steps are applied cumulatively. In panels A-C of Figure 4 the unfiltered Level 2 data are shown. The time-height plot (panels A and B in Figure 4) reveal a stratiform cloud passing over the site from 01:00 to 17:00 UTC followed by a series of low-level, most likely mixed-phase clouds. The short periodic gaps are due to interruptions of zenith observations by RHI scans of JOYRAD-35, and the large gap in DWR_{KaW} between 09 and 10 UTC results from missing JOYRAD-94 observations. The -15 °C isotherm (dashed line in the

20 time-height plots) marks a clear vertical separation between the DWRs, which remain around 0 dB for temperatures below -15 °C and rapidly increase for higher temperatures.

Panel C in Figure 4 is a 2D scatter density plot of DWR_{XKa} versus DWR_{KaW} (hereafter triple-frequency plot). The position of the measured data in the triple-frequency plot is mainly driven by the hydrometeors bulk density ρ and the mean volume diameter of the particle size distribution D_0 (see Kneifel et al. (2015) for more detail). This allows to discriminate between the

25 two snow processes: rimed particles follow the flat curve (low DWR_{XKa}) due to their higher density while aggregated particles give rise to a bending up signature (increase in DWR_{XKa} while DWR_{KaW} saturates or even decreases) due to their lower density, which is nicely shown in Figure 4, Panel C.

Apparently, a large number of points in Panel C, Figure 4 populate in areas which are unrealistic from a microphysical point, such as negative DWRs. Some of those originate from time periods when the offset can not be calculated or when the

30 correlation between the three radars is poor. Panels D and E in Figure 4 show the results after removing these data (bits 14 and 15 in the quality flag, see Table 4), an effect best visible between 17:00 and 20:00 for DWR_{KaW} and between 17:00 and 23:00 for DWR_{XKa}. This leads to a strong reduction of outliers from the aggregation signature in the triple-frequency space (Panel F in Figure 4).
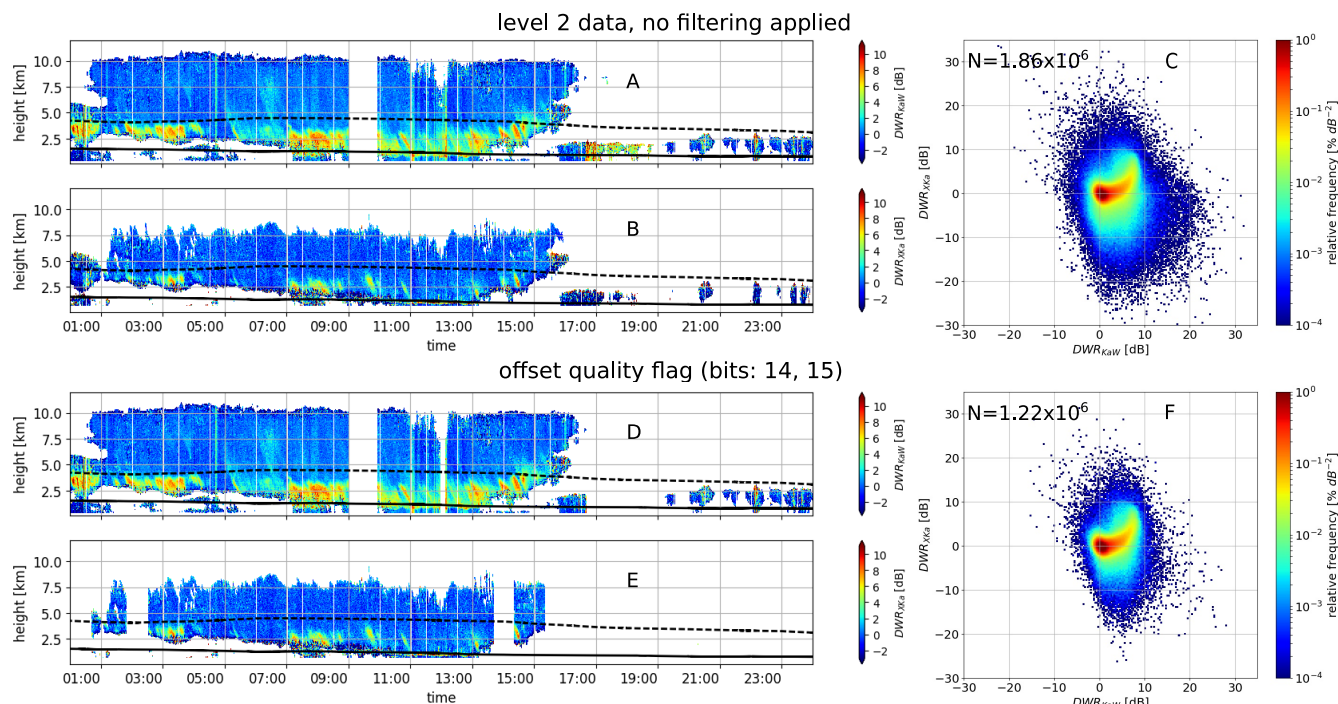
Figure 4. Time-height plots of DWR$_{KaW}$ (Panel A) and DWR$_{XKa}$ (Panel B) using the Level 2 data of 20.11.2015 without applying any filtering. The continuous line and dashed line are the isotherm of 0 and -15 °C, respectively provided by CloudNet products. The triple-frequency signatures for the ice part of the clouds are shown on the right (Panel C). Panels D-F show the data after applying the offset quality flags and restricted to data pairs with sufficient correlation. N in Panels C and F indicates the respective number of data pairs in the ice part of the clouds

Despite the data filtering described in the previous paragraph, the scatter around the main signature is still large. Panels A and B in Figure 5 show the time-height plots after removing observations flagged with the DWR 2-minute temporal variance flag (bit 13 in the quality flag, see Table 4). This filtering step removes most of the outliers from the aggregation signature in the triple-frequency plot (panel C in Figure 5). An additional 3-minutes running-window averaging of the reflectivities (panels

5   D and E in Figure 5) further removes the scatter and even more accentuates the aggregation signature in the triple-frequency space (panel F in Figure 5). The averaged reflectivities are not included in the TRIPEx dataset because it would not be possible to retrieve the original data from the mean values. The last two quality flags (bits 7 and 6, see Table 4) mark the data acquired during rainfall periods via the CloudNet product and times characterized by total liquid water path above 200 gm^{-2} measured by the microwave radiometer. Filtering according to these flags quite significantly reduces the amount of data (panel G and H

10   in Figure 5), but the aggregation signature clearly remains visible (panel I in Figure 5).
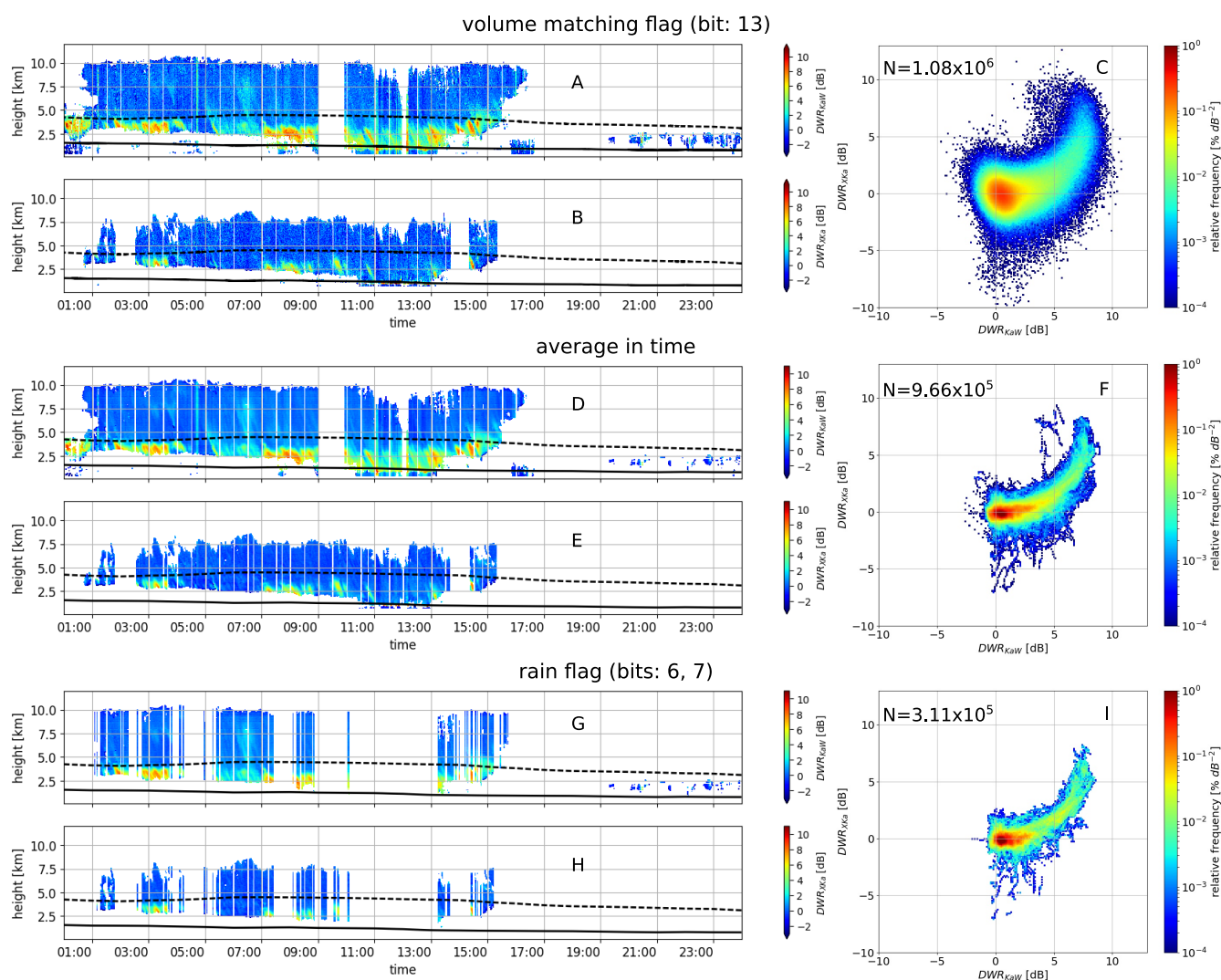
Figure 5. Same as Figure 4, but here the effects of cumulative data filtering subject to different quality flags and averaging is illustrated. Panels A-C display the effect of filtering based on the DWR variance in time, which removes areas potentially affected by bad radar volume matching. The effect of an additional temporal averaging over 3 minutes is shown in Panels E-F. The effect of the removal of time periods with rain as identified by CloudNet or large liquid water pathes measured by the nearby microwave radiometer are displayed in Panels G-I.

3.5 Radar sensitivity

The distribution of reflectivity values measured by the three radars during the entire campaign filtered with the error flags (bits 13, 14 and 15 in Table 4) and stratified by height above the site, is shown in Figure 6. As already mentioned, JOYRAD-35 and JOYRAD-94 show higher sensitivities compared to KiXPol up to high altitudes. JOYRAD-35 (Panel B in Figure 6) exhibits

5 the largest dynamic range compared to JOYRAD-94 and KiXPol (Panels A and B in Figure 6). The step-wise shape of the lowest altitude reflectivities from JOYRAD-94 is caused by different chirp settings (Table 2). A polynomial fit to the minimum retrieved linear reflectivities (Ze_{lin} in units of mm^6/m^3) as function of altitude z (units of m),

$$Ze_{lin}(z) = a \cdot z^b \tag{2}$$

results for KiXPol and JOYRAD-35 in the expected nearly quadratic decrease with range (Table 5). The slower decrease

10 (smaller exponent) for JOYRAD-94 results from the altitude-dependent sensitivity associated with the different chirp settings.

The melting layer was mostly observed at altitudes between 1 and 2 km which caused the kinks in the reflectivity distributions and their extremes in the KiXPol reflectivites. Although the KiXPol sensitivity did not allow to monitor the ice clouds above 7 km with reflectivities below -10 dBz, dual-wavelength studies of these clouds are still possible with the JOYRAD-94 and JOYRAD-35 included in the Level 2 data. Ice aggregation and riming processes however, which are the most relevant for triple-

15 frequency studies, usually occur at lower levels and larger reflectivities where all three radars provide sufficient sensitivity.
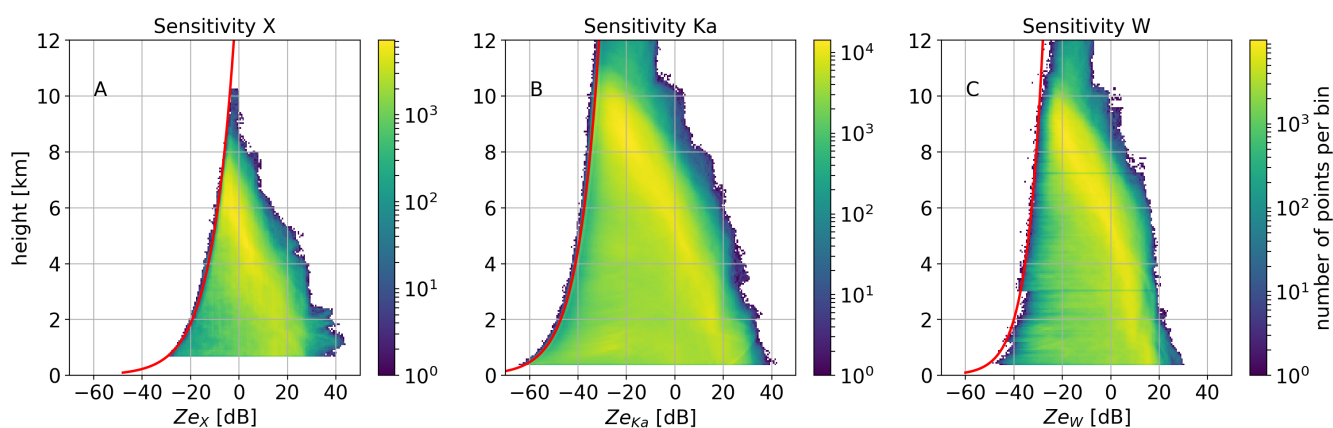

Figure 6. Histograms of reflectivities from the entire TRIPEx campaign Level 2 data for each radar. The red curve is the profile of the minimum retrieved reflectivity (Eq. 2). Panels A, B and C show the histograms for KiXPol, JOYRAD-35 and JOYRAD-94, respectively; all error flags (see Tab. 4) were applied to filter the data.

Table 5. Coefficients a and b for the sensitivity fit (Eq. 2) obtained for KiXPol, JOYRAD-35 and JOYRAD-94. The coefficients were calculated using the Level 2 dataset applying error flags (see Table 4).

	a	b
KiXPol	$6.25 \cdot 10^{-10}$	2.19
JOYRAD-35	$3.41 \cdot 10^{-12}$	2.04
JOYRAD-94	$8.36 \cdot 10^{-10}$	1.53

3.6 Limitations of the current dataset

Despite the processing steps to filter errors in the TRIPEx dataset discussed in Section 3.4 some limitations remain, which we discuss in this section in more detail. We identified on 23.11.2015 between 16:00 and 23:00 UTC enhanced Ze_X (-20 up to 10 dBZ) in the KiXPol observations (Figure 7, Panel A), while JOYRAD-35 (Ze_{Ka}) and Joyrad-95 (Ze_W) show no significant reflectivities. The mean Doppler velocity of that structure (MDV between 0 and 0.5 ms^{-1}) as observed by KiXPol slowly descends and is associated with strongly enhanced LDR from JOYRAD-35 (Figure 7, Panel B) and large Z_{dr} observed by the near-by scanning polarimetric X-band radar (JuXPol). The most likely explanation based on the polarimetric signature and the fall velocity are fall streaks of chaff, and therefore, these periods should be avoided for cloud microphysical studies. Also the scanning polarimetric X-Band radars (JuxPOL and BoXPOL) revealed very large ZDR values during that period (not shown).
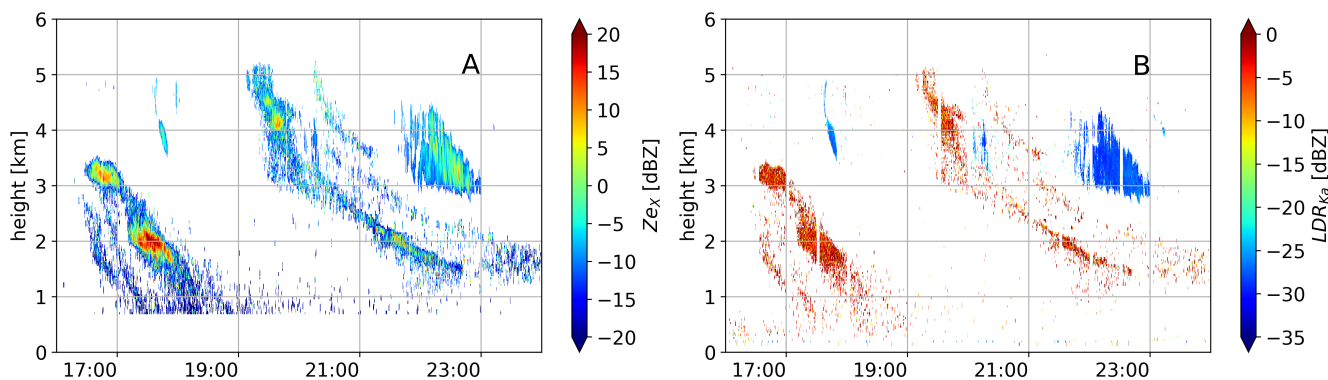
Figure 7. Time-height plots of the Ze_X and LDR_{Ka} of 23.11.2015 between 16:00 and 23:59. The region where the LDR is $\approx$ -5 dB is most probably a results of chaff. The JOYRAD-35 software applies a filtering for non-meteorological targets which removes most of the chaff; only the filtered JOYRAD-35 data are included in the TRIPEx dataset. Note, that no such filtering is applied to the KiXPol and JOYRAD-94 data.

One of the biggest challenges for multi-frequency observations is the match of radar volumes, which is negatively affected e.g. by horizontal instrument displacement, different radar beam widths and antenna pointing, and different range gates and temporal averaging. It is not trivial to accurately quantify these uncertainties, and their impact on multi-frequency studies also depends on the study target. For example, when analyzing cloud or precipitation structures with large vertical gradients (e.g.,

14

the melting layer) or high temporal variability, the volume mismatch effects will be larger than in studies of the usually more homogeneous ice clouds. In section 3.4.1 we provided some examples (Figure 5) on the application of error/quality flags and temporal averaging to mitigate these effects.
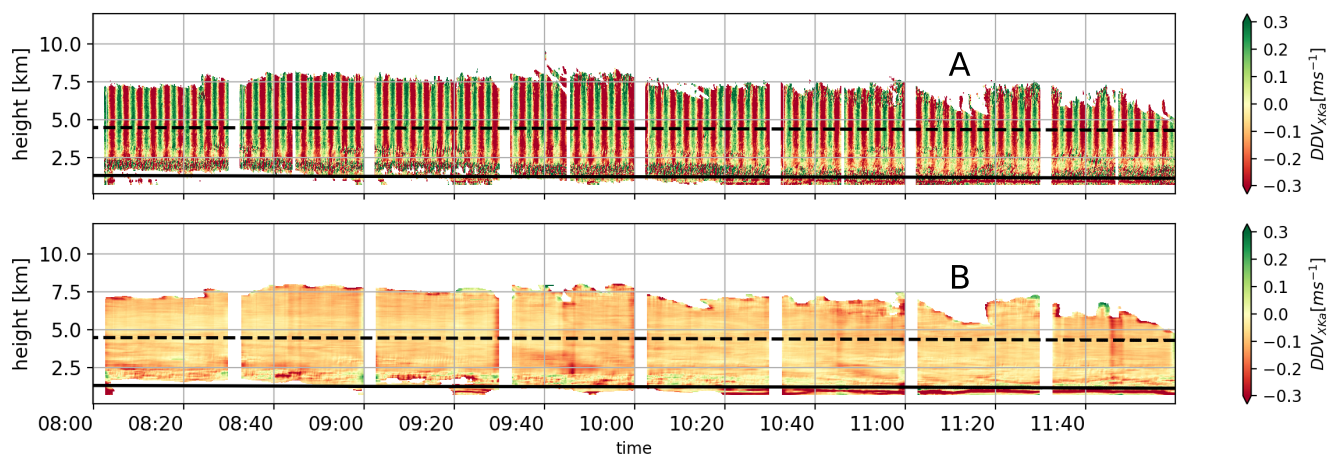

Figure 8. Time-height plots of the dual mean Doppler velocity using the Level 2 data of 20.11.2015. The dashed line and the continuous line are the isotherm of -15 and 0 °C, respectively. Panel A shows the DDV_{XKa} using the original data from Level 2. Panel B shows the DDV_{XKa} after applying the 3 minutes moving average.

Figure 8 illustrates effects related to imperfect vertical antenna pointing, which can be partly corrected for. When looking at
5   differences of vertical Doppler velocities between observations from low frequency and high frequency radars (Dual Doppler velocity, DDV), we expect an increases of the difference due to non-Rayleigh scattering effects (Matrosov, 2011; Kneifel et al., 2016). Large particles, which usually also have larger terminal velocities, have a lower reflectivity due to non-Rayleigh scattering effects. This effect also leads to a slightly lower MDV (e.g $MDV_X > MDV_{Ka} > MDV_W$). Since we expect mostly Rayleigh scatterers in the uppermost ice region of the cloud, the DDV should approach zero. However, for DDV_{XKa} (Panel A
10   of Figure 8) we find a periodic variation along the entire vertical range with the period matching the KiXPol scan duration of 3 minutes. Obviously a non-prefect zenith pointing of the KiXPol antenna introduces these periodic shifts in the mean Doppler velocity due to the contamination of the vertical Doppler signal by the horizontal wind component. We estimated the optimal averaging time window to eliminate this effect to 3 minutes by minimizing the standard deviation of DDV_{XKa} using different averaging window sizes (Panel B of Figure 8). Note, that we did not include the averaged data in the Level 2 data product
15   because the optimal averaging window depends on the prevailing atmospheric, height-dependent wind conditions, and original data cannot be recovered after averaging. We can also not completely rule out a slight mis-pointing of the other two radars, because their DDVs sometimes show deviations especially in regions with strong horizontal winds with maximum DDVs, however, below $0.4\,\mathrm{ms}^{-1}$. An ad-hoc estimate of the related relative radar mis-pointing using the horizontal wind information

from radiosondes for a few extreme cases suggest a potential mismatching of 0.5 °. A correction of the shift should be possible when reliable horizontal wind profiles are available, and it will be investigated in more details in the future.

4 Triple-frequency characteristics of ice and snow clouds

Long time series of observations are required in order to corroborate the significance and estimate the occurrence probability of certain process signatures in the triple-frequency space, which then can be used for the development of microphysical retrievals. Profound statistics of typical triple-frequency signatures will also help to constrain the scattering models, which are required for such retrievals. The currently available experimental datasets are restricted to short time periods or specific cases. Kulie et al. (2014) and Leinonen et al. (2012) used data collected during the Wakasa Bay campaign (Lobl et al., 2007) from Ku, Ka and W band airborne radars to evaluate the aggregate models and spheroidal snowflake models. Their derived values for DWR_{KaW} and DWR_{KuKa} reach up to $10\,\mathrm{dB}$ and $8\,\mathrm{dB}$, respectively. Although the data are rather noisy due to volume mismatch and attenuation effects, these were first observations which confirmed triple-frequency signatures which were so far only predicted by complex aggregate scattering models (Kneifel et al., 2011a). The first triple-frequency signatures from ground-based radars (C, Ka, W band) were presented by Stein et al. (2015) for two case studies. Similar to the Wakasa Bay studies, they found deviation from predictions based on simpler spheroidal-based scattering models; but their aggregates showed a DWR_{KaW} saturation around 8 dB and not a 'hook' or 'bending back' feature as found in the previous studies. They suggested this behaviour to be closely connected to a snow aggregate fractal dimension of two. Kneifel et al. (2015) combined triple-frequency ground-based radar (X, Ka and W band) with in-situ observations and analyzed three case studies with falling snow particles with different degrees of riming. For low density aggregates their DWR_{KaW} is also not exceeding the 8 dB limit reported by previous studies, but in addition they found a strong bending back feature (i.e., reduction of DWR_{KaW} for larger particles) with large DWR_{XKa} up to 15 dB. During riming periods, the triple-frequency signatures showed a distinctly different behavior. DWR_{KaW} increases up to 10 dBwhile DWR_{XKa} remains constant or slowly increases up to 3 dB, which appears in triple-frequency plots as an almost horizontal line.

The TRIPEx dataset is, to the best of our knowledge, one of the longest, quality-controlled triple-frequency data collection currently available, which allows to estimate the occurrence probability of several triple-frequency signatures in mid-latitudes winter clouds. In the following, we use the Level 2 data filtered only with the errors quality flag (see Table 4). The extension of the filtering to the warning flags would remove all melting layer cases or observations with larger amounts of super-cooled liquid water, which portray particularly interesting signatures of partially melted or rimed particles.

4.1 Temperature dependence of triple-frequency signatures

The large data set allows us to stratify the occurrence probaility of DWR_{KaW} (Panel A in Figure 9) and DWR_{XKa} (Panel B in Figure 9) according to air temperature, which results in four main regimes. The regime between -20 and -15 °C exhibits constant DWRs mostly below 3 dB. In the regime between -15 and -7.5 °C we find a rapid widening of the distribution to higher values in both DWRs. This suggests an increasing number of larger aggregates caused by stronger aggregation due

to preferential growth of dendritic particles around -15 °C; those particles are well known to favor aggregation due to their branched crystal structure. In accordance with previous studies, DWR_{KaW} saturates around 8 dB at -7.5 °C with only a small fraction reaching up to 10 dB. DWR_{XKa} approaches maximum values of 5 to 8 dB, however, the occurrence probability of enhanced DWR_{XKa} is smaller compared to those found for DWR_{KaW}. We expect this behavior as early aggregation is expected

5 to first enhance the DWR_{KaW} which is explained by the fact that growth of the particles first affect the high frequencies due to the transition from Rayleigh to non-Rayleigh regime. In our case, the W-Band radar is the first to be affect by this transition producing an enhance of DWR_{KaW}.

At temperatures warmer than -7.5 and colder than 0 °C, the distribution of DWR_{KaW} remains almost constant, except a small peak with higher values around -5 °C and widening of the distribution towards negative values. There are two main possible

10 sources for this widening. The first is the inter radar calibration correction (Sec 3.4) where offset calculated to the upper part of the clouds, the ice part, was used to correct the entire profile which may lead to overestimation of the Ze_W. The second possible source is the observation of different volumes by each radar due to a horizontal displacement and different range resolution; this effect is enhanced when the observed volumes are closer to the radar. Interestingly, DWR_{XKa} grows continuously up to 12 dB from temperatures warmer than -5 °C, which is in line with intensified aggregation of the snow particles towards lower

15 heights. The very large DWR_{XKa} in this regime can be explained by the increase of particle stickiness when approaching the 0 °C height. The fourth regime we define as regione between 0 °C and the maximum in LDR. At this regime the DWR_{KaW} show a trend to further increase while the DWR_{XKa} remain constant or are about to decrease. The DWR_{KaW} assumes values up to 10 dB while the DWR_{XKa} reaches values up to 15 dB which could be produced by a persistent aggregation formation.
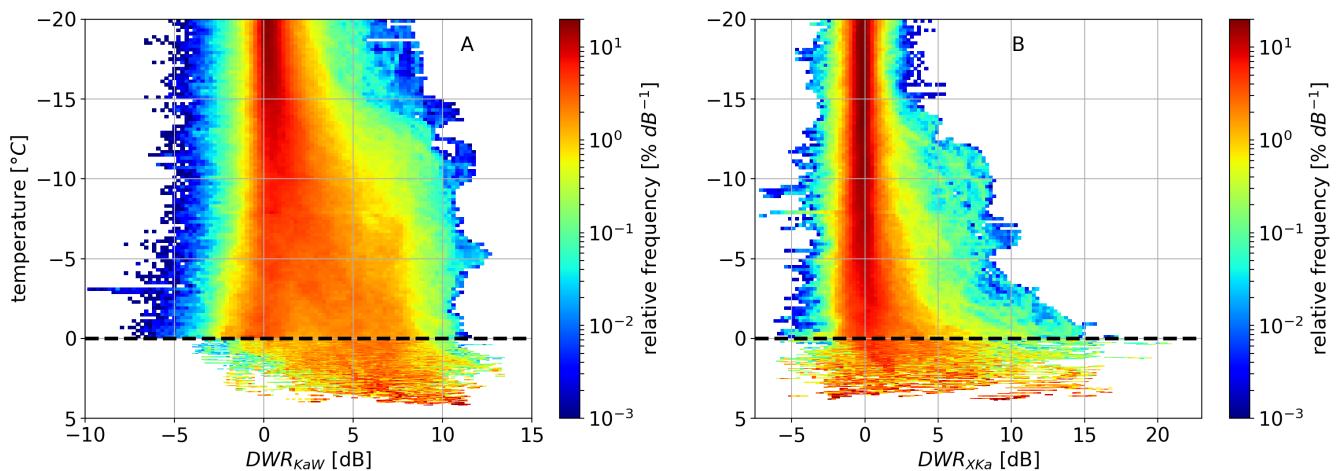

Figure 9. Two dimensional histograms (Contoured Frequency by Altitude Diagram, CFAD) of DWR as function of air temperature for the entire TRIPEx dataset. The dashed line indicates the isotherm of 0 °C. Be aware that the data below the dashed line is only for the cases when the melting layer was present. The DRWs were filtered using the error flags and averaged in time using a 3 minutes moving average. Panels A and B show the DWR_{KaW} and DWR_{XKa}, respectively.

The triple-frequency plots for the three temperature regimes unaffected by melting are shown in Figure 10. Panel A shows the data from the first regime (-20 to -15 °C) where the majority of the points are distributed around 0 for both DWRs. At this region the growth of the particles is mostly by vapor deposition producing a slightly increase of DWR_{KaW} up to 7 dB. In Panel B, the data from the second regime (-15 to -7.5 °C) are from the region where larger aggregates are likely generated

5   in the dendritic growth layer. Similar to e.g. Stein et al. (2015), we find the typical bending or hook signature saturating at about a DWR_{KaW} of 8 dB. Although we combine different clouds, the variability of the triple-frequency signatures is relatively small. For warmer temperatures (-7.5 to -1 °C (Panel C), where needle aggregates are generated and ice particles start to become more sticky, the bending feature becomes more pronounced. For DWR_{XKa} reaching up to 12 dB also the bending back signature (reduction of DWR_{KaW} with increasing DWR_{XKa} as reported in Kneifel et al. (2015)) becomes visible for parts

10 of the data set. This panel also reveals a secondary mode with DWR_{XKa} below 3 dB and DWR_{KaW} reaching up to 12 dB. Following Kneifel et al. (2015), this mode could hint at rimed particles, which are too small to enhance DWR_{XKa}, but due to their increased density and hence larger refractive index increase DWR_{KaW}. We will investigate this feature in more detail in the next subsection.

The dataset contains particularly large DWR signatures close to 0 °C and at higher temperatures, which could be caused by

15 melting snowflakes or simply by enhanced aggregation. To further investigate this signature we generated the triple-frequency plot for the data between the 0 °C and the height of the maximum in the LDR, which we consider as a proxy for the center of the melting layer (Le and Chandrasekar, 2013) (Figure 11). In this region DWR_{XKa} reaches maximum values up to 20 dB already at low DWR_{KaW}. Overall, the data points are much more scattered than those in the colder temperature regions, which also might result from effects of radar volume mismatch caused by the stronger vertical gradients near the melting

20 layer; another possibility for this effect is the much lower number of data. Latent heat release by melting increases turbulent motions, which might further enhance detrimental effects of volume mismatch. We need to be careful in interpreting these features as triple-frequency signatures of the melting layer, because the temperature information is based on CloudNet product which obtains the temperature from ECMWF analysis which cannot be expected to represent small scale variations of the 0 °C isotherm. Moreover, melting can be delayed depending on the profile of temperature and humidity, and on the density and size

25 of the particles themselves (Matsuo and Sasyo, 1981; Rasmussen and Pruppacher, 1982). A sagging of the melting layer has been repeatedly observed with the scanning polarimetric X-band radar in Bonn (BoXPol also part of JOYCE-CF) in case of dominant riming processes (Xie et al., 2016; Trömel et al., 2018). Rimed particles fall with higher terminal velocities and melt at lower heights. In the following subsection we will use LDR and the mean Doppler velocity to better separate non-melted from melted snow particles.

30 ## 4.2 Signatures of riming and melting snow particles

During riming, super-cooled liquid water droplets freeze onto the ice particles, which strongly increases the particle mass while its size grows only slowly, especially during the onset of riming. Since the terminal velocity is mainly governed by the relation of particle mass (gravitational force) and its cross section perpendicular to the air stream (drag force), its terminal and mean Doppler velocity (MDV) increase due to riming (Mosimann (1995)). MDVs above $1.5 \ \mathrm{ms}^{-1}$ can be used as a simple indicator
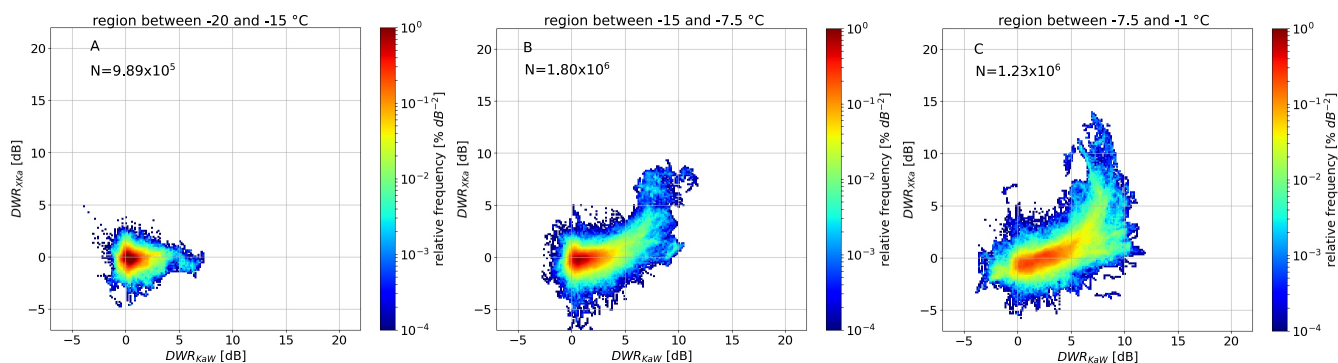
Figure 10. Two dimensional histogram of the triple frequency signatures for different temperature regions normalized by the total number of points N. The color shows the relative frequency. Panel A is for region between -20 °C and -15 °C; Panel B shows the region between -15 °C and -7.5 °C; Panel C illustrates data points lying between -7.5 °C and -1 °C.
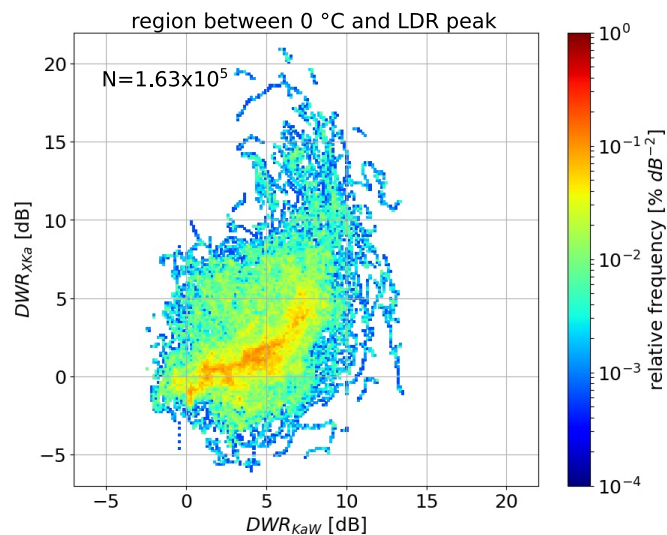
Figure 11. Two dimensional histogram of the triple frequency signatures for a region between 0 °C and the maximum of LDR in the melting layer normalized by the total number of points N. The color shows the relative frequency.

of rimed particles as long as vertical air motions are small (e.g. Mosimann (1995)). The fraction of triple-frequency data in the temperature range between -20 and -1 °C with MDV larger than 1.5 ms^{-1} is about 1.3% and displayed in Figure 12. Interestingly, we find one mode which appears to be very similar to a line with low slope found for rimed particles in Kneifel et al. (2015), which coincides with large MDVs up to 2.4 ms^{-1} and DWR$_{KaW}$ up to 10 dB. However, the correlation between enhanced DWR$_{KaW}$ and MDV is less clear than in the case shown in Kneifel et al. (2015). A more detailed investigation showed that TRIPEx contains only two short riming periods of a few minutes duration, while the period analyzed by Kneifel et al. (2015) was considerable longer ($\approx$ 20 min). In general, DWR$_{KaW}$ is expected to increase for larger particle sizes and strong riming, but detailed sensitivity studies which clearly characterize these dependencies are still missing. Another mode in Figure 12 with larger DWR$_{XKa}$ of about 3 dB suggest mean particles sizes exceeding 8 mm according to Kneifel et al. (2015). We speculate, that this mode might be related to only slightly rimed aggregates. A larger number of riming events is required to better investigate the sensitivities of MDV and triple-frequency signatures to various degrees of riming, which also would be a very valuable basis to constrain theoretical particle models as e.g. developed by Leinonen and Szyrmer (2015).
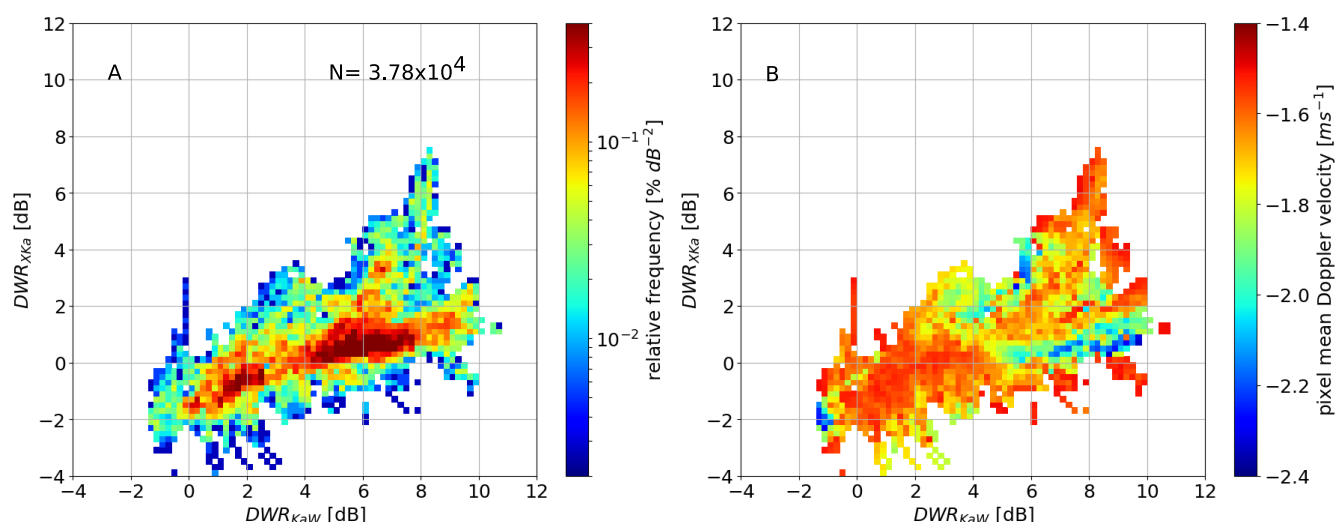

Figure 12. Triple frequency signatures for Level 2 data with temperatures between -20 and -1 °C and a mean Doppler velocity (MDV) above 1.5 ms^{-1} in order to select potentially riming particles. Panel A shows the relative frequency of the observations; Panel B indicates the average MDV of each pixel in the histogram.

A particularly interesting signature shown in Figure 11 are the very large DWR$_{XKa}$ close to the melting layer. To the author's knowledge these features have not yet been described, nor is it clear whether these signatures are caused by very large aggregates or melting particles. A pure melting of snowflakes should enhance the MDV because of their decrease in size (and thus cross sectional area) and drag in the airflow. Early melting can, however, be better detected by LDR: the much larger refractive index of liquid water compared to ice and the initially still asymmetric melting snowflake result in a much larger depolarization signal as for the dry snowflake. Hence, we re-plot Figure 11. One can clearly see the transition from dry snowflakes with

typical MDV of 1 ms^{-1} and LDR values around -15 dB to larger MDV and coinciding rising LDR as expected for melted snow. Interestingly, the very large DWR$_{XKa}$ show mostly MDV and LDR values associated to unmelted snowflakes. Once the MDV and LDR indicate onset of melting, the DWR, especially the DWR$_{XKa}$, rapidly decrease. As the DWR$_{XKa}$ is strongly related to the mean particle size, the results indicate that the largest snowflake sizes occur before the melting starts. Once the snowflakes are completely melted, the DWR$_{KaW}$ will be still enhanced due to non-Rayleigh scattering of the raindrops but the DWR$_{XKa}$ will be close to 0 dB (Tridon et al., 2017). However, our corrections for attenuation within the melting layer are certainly incomplete, thus we leave a deeper analysis of that feature to future studies.
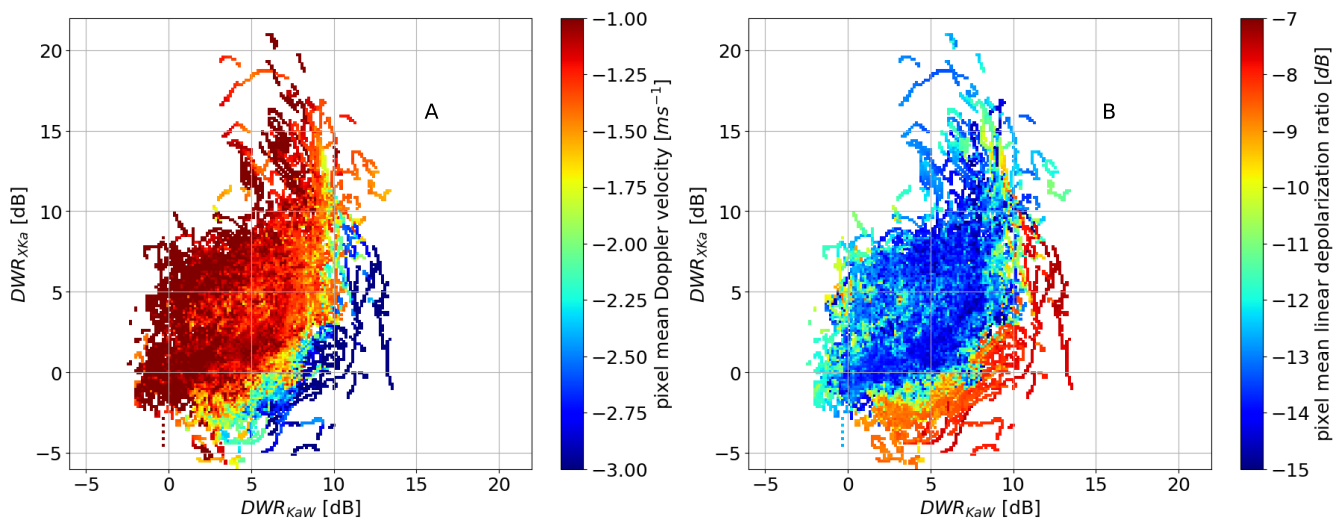
Figure 13. Triple-frequency diagrams of observations between 0 °C and the maximum of LDR in the melting layer (same as Panel C of Figure 10), but the color in Panel A indicates the average MDV while in Panel B the color shows the average LDR.

5 Conclusions

This paper presents the first long-term dataset (two months) of vertically pointing triple-frequency Doppler radar (X, Ka, and W-Band) observations of winter clouds at a mid-latitude site (JOYCE-CF, Jülich, Germany), and it describes the spatio-temporal re-gridding of the data as well as the offset and attenuation corrections applied. Several quality flags are developed which enables to filter the dataset according to specific application. The quality flags have been separated into error and warning flags; we recommend to always apply the error flags while the warning flags might not be necessary depending on the case or the focus of the analysis. All corrections applied are separately stored in the data files in order to allow the user to recover and work with data at intermediate processing steps and to potentially apply individual and other corrections. This might be necessary as our focus was on the ice and snow part of the cloud and hence, for example the correction for path integrated attenuation might be inappropriate for studies investigating the melting layer or rainfall.

The statistical analysis of the ice part of the clouds revealed dominant triple-frequency signatures related to aggregation (hook or bending up feature). In agreement with previous studies, DWR_{KaW} mostly saturates around 8 dB while DWR_{XKa} reaches values of up to 20 dB in regions of presumably intense aggregation close to the melting layer. Due to the large dataset, we were able to investigate the relation between the DWRs and temperature. The first significant increase of aggregation starts

5   at -15 °C where plate-like and dendritic crystals are known to grow efficiently and favour aggregation. In this zone DWR_{KaW} mostly increases up to its saturation value of 8 dB while DWR_{XKa} increases mainly below -7.5 °C. Close to the melting layer DWR_{XKa} massively increases up to extreme values of 20 dB, which has not been reported so far. A further investigation using LDR and MDV revealed that these extreme DWR_{XKa} are indeed due to large dry aggregates rather than melting particles, which cause the DWR_{XKa} to decrease. This finding suggests future studies of the aggregation processes within or close to the melting

10   layer, but also scattering computations of melting particles. Although the dataset contains only a few short riming periods (approximately 1.3% of the data between -20 and -1 °C), simple MDV threshold reveals the typical riming signature (flat horizontal line in the triple-frequency space) reported for riming case studies in Kneifel et al. (2015). The statistical analysis of riming is more challenging as compared to aggregation. Riming is often connected to larger amounts of super-cooled liquid water, larger vertical air motions, and turbulence, which deteriorate the signal due to liquid water attenuation and enhance

15   effects of imperfect radar volume matching. Riming could be further investigated with this dataset when concentrating on specific cases where specific corrections and filtering can be applied.

The synergy with nearby polarimetric weather radar observations will be investigated in future studies by including the vertical polarimetric profiles matching the JOYCE-CF site based on Quasi-Vertical Profiles (QVPs) (e.g. Trömel et al. (2014); Ryzhkov et al. (2016)) or Columnar Vertical Profiles (CVPs) (Murphy et al., 2017; Trömel et al., 2018). Also a data release

20   including the W and Ka Band Radar Doppler spectra is planned.

6   Data availability

The TRIPEx Level 2 data are available for download at the ZENODO platform DOI: 10.5281/zenodo.1405539. Quicklooks of the TRIPEx dataset are freely accessible via a data quicklook browser http://gop.meteo.uni-koeln.de/~hatpro/dataBrowser/ dataBrowser2.html. The raw and Level 1 data can be requested from the corresponding author.

References

Görsdorf, U., Lehmann, V., Bauer-Pfundstein, M., Peters, G., Vavriv, D., Vinogradov, V., and Volkov, V.: A 35-GHz polarimetric doppler radar for long-term observations of cloud parameters-description of system and data processing, Journal of Atmospheric and Oceanic Technology, 32, 675–690, https://doi.org/10.1175/JTECH-D-14-00066.1, 2015.

5 Hogan, R. J., Illingworth, A. J., and Sauvageot, H.: Measuring crystal size in cirrus using 35- and 94-GHz radars, Journal of Atmospheric and Oceanic Technology, 17, 27–37, https://doi.org/10.1175/1520-0426(2000)017<0027:MCSICU>2.0.CO;2, 2000.

Hogan, R. J., Gaussiat, N., and Illingworth, A. J.: Stratocumulus Liquid Water Content from Dual-Wavelength Radar, Journal of Atmospheric and Oceanic Technology, 22, 1207–1218, https://doi.org/10.1175/JTECH1768.1, 2005.

Hou, A., Kakar, R., Neeck, S., Azarbarzin, A., Kummerow, C., Kojima, M., Oki, R., Nakamura, K., and Iguchi, T.: The Global Precipitation
10 Measurement Mission, Bulletin of the American Meteorological Society, 95, 701–722, https://doi.org/10.1175/BAMS-D-13-00164.1, 2014.

Huang, G.-J., Bringi, V. N., and Thurai, M.: Orientation Angle Distributions of Drops after an 80-m Fall Using a 2D Video Disdrometer, Journal of Atmospheric and Oceanic Technology, 25, 1717–1723, https://doi.org/10.1175/2008JTECHA1075.1, 2008.

Illingworth, A. J., Hogan, R. J., O'Connor, E. J., Bouniol, D., Brooks, M. E., Delanoë, J., Donovan, D. P., Eastment, J. D., Gaussiat, N.,
15 Goddard, J. W. F., Haeffelin, M., Klein Baltink, H., Krasnov, O. A., Pelon, J., Piriou, J. M., Protat, A., Russchenberg, H. W. J., Seifert, A., Tompkins, A. M., van Zadelhoff, G. J., Vinit, F., Willen, U., Wilson, D. R., and Wrench, C. L.: Cloudnet: Continuous evaluation of cloud profiles in seven operational models using ground-based observations, Bulletin of the American Meteorological Society, 88, 883–898, https://doi.org/10.1175/BAMS-88-6-883, 2007.

Kalthoff, N., Adler, B., Wieser, A., Kohler, M., Träumner, K., Handwerker, J., Corsmeier, U., Khodayar, S., Lambert, D., Kopmann, A.,
20 Kunka, N., Dick, G., Ramatschi, M., Wickert, J., and Kottmeier, C.: KITcube - a mobile observation platform for convection studies deployed during HyMeX, Meteorologische Zeitschrift, 22, 633–647, http://dx.doi.org/10.1127/0941-2948/2013/0542, 2013.

Kneifel, S., Kulie, M. S., and Bennartz, R.: A triple-frequency approach to retrieve microphysical snowfall parameters, Journal of Geophysical Research Atmospheres, 116, 1–15, https://doi.org/10.1029/2010JD015430, 2011a.

Kneifel, S., Maahn, M., Peters, G., and Simmer, C.: Observation of snowfall with a low-power FM-CW K-band radar (Micro Rain Radar),
25 Meteorology and Atmospheric Physics, 113, 75–87, https://doi.org/10.1007/s00703-011-0142-z, 2011b.

Kneifel, S., von Lerber, A., Tiira, J., Moisseev, D., Kollias, P., and Leinonen, J.: Observed relations between snowfall microphysics and triple-frequency radar measurements, Journal of Geophysical Research: Atmospheres, 120, 6034–6055, https://doi.org/10.1002/2015JD023156, http://doi.wiley.com/10.1002/2015JD023156, 2015.

Kneifel, S., Kollias, P., Battaglia, A., Leinonen, J., Maahn, M., Kalesse, H., and Tridon, F.: First observations of triple-
30 frequency radar Doppler spectra in snowfall: Interpretation and applications, Geophysical Research Letters, 43, 2225–2233, https://doi.org/10.1002/2015GL067618, 2016.

Küchler, N., Kneifel, S., Löhnert, U., Kollias, P., Czekala, H., and Rose, T.: A W-band radar-radiometer system for accurate and continuous monitoring of clouds and precipitation, Journal of Atmospheric and Oceanic Technology, 34, 2375–2392, https://doi.org/10.1175/JTECH-D-17-0019.1, 2017.

35 Kulie, M. S., Hiley, M. J., Bennartz, R., Kneifel, S., and Tanelli, S.: Triple-Frequency Radar Reflectivity Signatures of Snow: Observations and Comparisons with Theoretical Ice Particle Scattering Models, J. Appl. Meteorol. Climatol., 53, 1080–1098, 2014.

Le, M. and Chandrasekar, V.: Hydrometeor profile characterization method for dual-frequency precipitation radar onboard the GPM, IEEE Transactions on Geoscience and Remote Sensing, 51, 3648–3658, https://doi.org/10.1109/TGRS.2012.2224352, 2013.

Leinonen, J.: High-level interface to T-matrix scattering calculations: architecture, capabilities and limitations, Opt. Express, 22, 1655–1660, https://doi.org/10.1364/OE.22.001655, http://www.opticsexpress.org/abstract.cfm?URI=oe-22-2-1655, 2014.

Leinonen, J. and Moisseev, D.: What do triple-frequency radar signatures reveal about aggregate snowflakes?, J. Geophys. Res., 120, 229–239, http://dx.doi.org/10.1002/2014JD022072, 2015.

Leinonen, J. and Szyrmer, W.: Radar signatures of snowflake riming: a modeling study, Earth and Space Science, pp. 2333–5084, https://doi.org/10.1002/2015EA000102, 2015.

Leinonen, J., Kneifel, S., Moisseev, D., Tyynelä, J., Tanelli, S., and Nousiainen, T.: Evidence of nonspheroidal behavior in millimeter-wavelength radar observations of snowfall, Journal of Geophysical Research Atmospheres, 117, 1–10, https://doi.org/10.1029/2012JD017680, 2012.

Lobl, E. S., Aonashi, K., Murakami, M., Griffith, B., Kummerow, C., Liu, G., and Wilheit, T.: Wakasa bay, Organization, pp. 551–558, https://doi.org/10.1175/BAMS-88-4-551, 2007.

Löffler-Mang, M. and Joss, J.: An optical disdrometer for measuring size and velocity of hydrometeors, Journal of Atmospheric and Oceanic Technology, 17, 130–139, https://doi.org/10.1175/1520-0426(2000)017<0130:AODFMS>2.0.CO;2, 2000.

Löhnert, U., Schween, J. H., Acquistapace, C., Ebell, K., Maahn, M., Barrera-Verdejo, M., Hirsikko, A., Bohn, B., Knaps, A., O'Connor, E., Simmer, C., Wahner, A., and Crewell, S.: JOYCE: Jülich Observatory for Cloud Evolution, Bulletin of the American Meteorological Society, 96, 1157–1174, https://doi.org/10.1175/BAMS-D-14-00105.1, 2015.

Maahn, M., Löhnert, U., Kollias, P., Jackson, R. C., and McFarquhar, G. M.: Developing and evaluating ice cloud parameterizations for forward modeling of radar moments using in situ aircraft observations, Journal of Atmospheric and Oceanic Technology, 32, 880–903, https://doi.org/10.1175/JTECH-D-14-00112.1, 2015.

Matrosov, S. Y.: Possibilities of cirrus particle sizing from dual-frequency radar measurements, Journal of Geophysical Research, 98, 20 675, https://doi.org/10.1029/93JD02335, 1993.

Matrosov, S. Y.: A dual-wavelength radar method to measure snowfall rate, J. Appl. Meteorol., 37, 1510–1521, 1998.

Matrosov, S. Y.: Feasibility of using radar differential Doppler velocity and dual-frequency ratio for sizing particles in thick ice clouds, Journal of Geophysical Research, 116, D17 202, https://doi.org/10.1029/2011JD015857, http://doi.wiley.com/10.1029/2011JD015857, 2011.

Matsuo, T. and Sasyo, Y.: Melting of Snowflakes below Freezing Level in the Atmosphere, Journal of the Meteorological Society of Japan. Ser. II, 59, 10–25, https://doi.org/10.2151/jmsj1965.59.1_10, 1981.

Mosimann, L.: An improved method for determining the degree of snow crystal riming by vertical Doppler radar, Atmospheric Research, 37, 305–323, https://doi.org/10.1016/0169-8095(94)00050-N, 1995.

Murphy, A., Ryzhkov, A., Zhang, P., McFarquhar, G., Wu, W., and Stechman, D.: A Polarimetric and Microphysical Analysis of the Stratiform Rain Region of MCSs, in: 38th Conference on Radar Meteorology, Chicago, Illinois, USA, 2017.

Rasmussen, R. and Pruppacher, H. R.: A wind tunnel and theoretical study of the melting behavior of atmospheric ice particles I: A wind tunnel study of frozen drops of radius < 500 μm, https://doi.org/10.1175/1520-0469(1982)039<0152:AWTATS>2.0.CO;2, 1982.

Rosenkranz, P. W.: Water vapor microwave continuum absorption: A comparison of measurements and models, Radio Science, 33, 919–928, http://doi.wiley.com/10.1029/98RS01182, 1998.

Ryzhkov, A., Zhang, P., Reeves, H., Kumjian, M., Tschallener, T., Trömel, S., and Simmer, C.: Quasi-vertical profiles-A new way to look at polarimetric radar data, Journal of Atmospheric and Oceanic Technology, 33, 551–562, https://doi.org/10.1175/JTECH-D-15-0020.1, 2016.

Simmer, C., Thiele-Eich, I., Masbou, M., Amelung, W., Bogena, H., Crewell, S., Diekkrüger, B., Ewert, F., Hendricks Franssen, H.-J., Huisman, J. A., Kemna, A., Klitzsch, N., Kollet, S., Langensiepen, M., Löhnert, U., Rahman, A. S. M. M., Rascher, U., Schneider, K., Schween, J., Shao, Y., Shrestha, P., Stiebler, M., Sulis, M., Vanderborght, J., Vereecken, H., van der Kruk, J., Waldhoff, G., and Zerenner, T.: Monitoring and Modeling the Terrestrial System from Pores to Catchments: The Transregional Collaborative Research Center on Patterns in the Soil–Vegetation–Atmosphere System, Bulletin of the American Meteorological Society, 96, 1765–1787, https://doi.org/10.1175/BAMS-D-13-00134.1, 2015.

Stein, T. H., Westbrook, C. D., and Nicol, J. C.: Fractal geometry of aggregate snowflakes revealed by triple-wavelength radar measurements, Geophysical Research Letters, 42, 176–183, https://doi.org/10.1002/2014GL062170, 2015.

Thurai, M., Huang, G. J., Bringi, V. N., Randeu, W. L., and Schönhuber, M.: Drop Shapes, Model Comparisons, and Calculations of Polarimetric Radar Parameters in Rain, Journal of Atmospheric and Oceanic Technology, 24, 1019–1032, https://doi.org/10.1175/JTECH2051.1, 2007.

Tridon, F., Battaglia, A., Luke, E., and Kollias, P.: Rain retrieval from dual-frequency radar Doppler spectra: validation and potential for a mid-latitude precipitating case-study, Quarterly Journal of the Royal Meteorological Society, 143, 1364–1380, https://doi.org/10.1002/qj.3010, http://doi.wiley.com/10.1002/qj.3010, 2017.

Trömel, S., Ryzhkov, A. V., Zhang, P., and Simmer, C.: Investigations of backscatter differential phase in the melting layer, Journal of Applied Meteorology and Climatology, 53, 2344–2359, https://doi.org/10.1175/JAMC-D-14-0050.1, 2014.

Trömel, S., Ryzhkov, A., Hickman, B., Mühlbauer, K., and Simmer, C.: Climatology of the vertical profiles of polarimetric radar variables at X band in stratiform clouds, Submitted to Journal of Applied Meteorology and Climatology, 2018.

Tyynelä, J. and Chandrasekar, V.: Characterizing falling snow using multifrequency dual-polarization measurements, J. Geophys. Res., 119, https://doi.org/10.1002/2013JD021369, 2014.

Xie, X., Evaristo, R., Simmer, C., Handwerker, J., and Trömel, S.: Precipitation and microphysical processes observed by three polarimetric X-band radars and ground-based instrumentation during HOPE, Atmospheric Chemistry and Physics, 16, 7105–7116, https://doi.org/10.5194/acp-16-7105-2016, 2016.

Zacharias, S., Bogena, H., Samaniego, L., Mauder, M., Fuß, R., Pütz, T., Frenzel, M., Schwank, M., Baessler, C., Butterbach-Bahl, K., Bens, O., Borg, E., Brauer, A., Dietrich, P., Hajnsek, I., Helle, G., Kiese, R., Kunstmann, H., Klotz, S., Munch, J. C., Papen, H., Priesack, E., Schmid, H. P., Steinbrecher, R., Rosenbaum, U., Teutsch, G., and Vereecken, H.: A Network of Terrestrial Environmental Observatories in Germany, Vadose Zone Journal, 10, 955, https://doi.org/10.2136/vzj2010.0139, 2011.